Bulletin of the Seismological Society of America, Vol. 96, No. 5, pp. 1779–1794, October 2006, doi: 10.1785/0120050219

Modeling of the Perfectly Matched Layer Absorbing Boundaries and Intrinsic Attenuation in Explicit Finite-Element Methods

by Shuo Ma* and Pengcheng Liu

Abstract We present an implementation of the perfectly matched layer (PML) absorbing boundary conditions and modeling of intrinsic attenuation (Q) in explicit finite-element simulations of wave propagation. The finite-element method uses one integration point and an hourglass control scheme, which leads to an easy extension of the velocity-stress implementation of PML to the finite-element method. Numerical examples using both regular and irregular elements in the PML region show excellent results: very few reflections are observed from the boundary for both body waves and surface waves—far superior to the classic first-order absorbing boundaries. The one-point integration also gives rise to an easy incorporation of the coarse-grain approach for modeling Q (Day, 1998). We implement the coarse-grain method in a structured finite-element mesh straightforwardly. We also apply the coarse-grain method to a widely used, slightly unstructured finite-element mesh, where unstructured finite elements are only used in the vertical velocity transition zones. A linear combination of eight relaxation mechanisms is used to simulate the target attenuation model over a wide frequency range. The relaxation time and weight of each relaxation mechanism are distributed in a spatially periodic manner to the center of each element. Stress relaxations caused by anelastic material response are calculated from elastic strains in the element and redistributed to the nodal forces of the element. Numerical simulation of anelastic wave propagation in a layered velocity structure with very small Qs using both the structured mesh and the unstructured mesh show excellent agreement with the analytical solutions when the viscoelastic modulus is calculated by a harmonic average over the coarse-grain unit. Our scheme greatly expands the use of PML and the coarse-grain method for modeling Q, so that these methods can be used in a versatile and efficient finite-element formulation.

Introduction

As one of the most popular methods in the engineering community, the finite-element method is increasingly applied in the simulation of wave propagations (e.g., Lysmer and Drake, 1972; Smith, 1975; Pereyra *et al.*, 1992; Bao *et al.*, 1998; Hisada *et al.*, 1998; Kim *et al.*, 2003; Koketsu *et al.*, 2004) and earthquake dynamic rupture propagations (e.g., Archuleta and Frazier, 1978; Day, 1982; Oglesby *et al.*, 1998; Aagaard *et al.*, 2001; Anderson *et al.*, 2003). The finite-element method allows the use of irregular elements of different size, geometry, and order of approximations, which make it very efficient to model complicated geometrical boundary conditions. For example, when dealing with free-surface topography and nonplanar fault surfaces, the finite-element method is far superior to the widely used finite-difference method.

Among different finite-element implementations, the explicit finite-element method with second-order elements and one-point integration is widely used. It combines the flexibility of the finite-element method and the efficiency of the finite-difference method. Because of its efficiency and versatility, this method has been widely implemented and extensively applied to transient analyses in engineering and seismology. In this article, for brevity, we refer to this particular implementation as the finite-element method.

The underlying algorithm for the explicit finite-element method is simple. In most cases, it uses four-node quadrilateral elements in two dimensions and eight-node hexahedral elements in three dimensions and employs one integration point and an hourglass control scheme. Higher-order elements are rarely used in transient analyses because of the computational costs and the numerical noise resulting from the *ad hoc* mass lumping necessary to generate a diagonal mass matrix (Hughes, 1987). One-point integration provides

*Present address: Department of Geophysics, Stanford University, Panama Mall 397, Stanford, California 94305-2215.

tremendous computational benefits in dynamic simulations. There is a 3/4 reduction in computational time in two dimensions and 7/8 reduction in three dimensions with the one-point integration compared with the full integration. One-point integration also gives rise to an efficient way to simulate nonlinear material response (Goudreau and Hallquist, 1982), whereas it is cumbersome for fully integrated elements. Furthermore, the fully integrated elements tend to lock if the material becomes incompressible.

One major drawback of one-point integration in the elements, as used in our implementation, is a mesh instability known as hourglassing. However, the hourglass modes can be eliminated by well-developed hourglass control schemes (e.g., Kosloff and Frazier, 1978; Flanagan and Belytschko, 1981; Belytschko *et al.*, 1984). Kosloff and Frazier (1978) identified the similarity of their hourglass control and the incompatible element of Wilson *et al.* (1973), and showed that a one-point integration implementation coupled with a stiffness hourglass control scheme can produce a more accurate flexural response than fully integrated elements. Considering the large cost savings and desirable features of one-point integration, fully integrated elements are often avoided in transient analysis. In this article, we will show that the widely used one-point integration scheme leads to an easy implementation of the perfectly matched layer (PML) absorbing boundary (Bérenger, 1994, 1996) and an efficient incorporation of seismic attenuation in the explicit finite-element method.

PML

For waves in unbounded domains, the computational domain must be truncated to keep the computation tractable. Absorbing boundaries are usually placed around the region of interest so that when the outgoing waves impinge on the boundaries the reflection is minimal, thus mimicking the nature of wave propagations in unbounded domains. Classical absorbing boundary conditions (ABCs) based on a paraxial approximation are widely used in the finite-element community (e.g., Lysmer and Kuhlmeyer, 1969; Clayton and Engquist, 1977; Higdon, 1991). These ABCs can be easily implemented and when the incident angle is normal to the boundary they can absorb high-frequency waves well. They reflect a large amount of spurious energy at grazing incidence in addition to low-frequency energy at all angles of incidence, however. Moreover, they absorb surface waves rather poorly. Bérenger (1994, 1996) first introduced the PML absorbing boundary for electromagnetic waves, which has the remarkable property of having zero reflection coefficients for almost all angles of incidence and all frequencies before discretization. This formulation has proved to be extremely efficient and has become popular. Soon after their introduction, PMLs were applied to elastic wave propagation (e.g., Hastings *et al.*, 1996; Collino and Tsogka, 2001; Marcinkovich and Olsen, 2003; Festa and Nielsen, 2003; Komatitsch and Tromp, 2003; Basu and Chopra, 2004; Festa and Vilotte, 2005). Collino and Tsogka (2001) first presented a velocity-stress formulation of PML for the elastic wave equation, which serves as the basis for the 3D staggered-grid velocity-stress finite-difference implementation of Marcinkovich and Olsen (2003) and Festa and Nielsen (2003). Komatitsch and Tromp (2003) extended the velocity-stress implementation of PML to the second-order wave equations, which can be used by the finite-element and spectral-element methods, but their implementation is not straightforward. A third-order differential equation must be solved at every timestep, which necessitates modification of the numerical algorithm in the interior region. In this article, we show that the one-point integration leads to an easy extension of the velocity-stress implementation of PML to the explicit finite-element method, which allows the use of irregular elements in the PML region.

Seismic Attenuation

Energy loss through nonelastic process is usually measured by intrinsic attenuation and parameterized with the quality factor Q. Incorporation of seismic Q in the ground-motion modeling is important because it can strongly affect the amplitude and duration of the ground motion when waves travel within shallow soft materials. Seismic Q also decreases the waveform amplitudes and causes strong waveform dispersions (Aki and Richards, 2002) when waves travel over regional/global distances.

Rayleigh damping is widely used in the finite-element modeling of structural dynamics to model the energy-loss mechanism in the structures. It has also been applied in the strong ground motion modeling for the incorporation of seismic-wave attenuation (Bao *et al.*, 1998). However, Rayleigh damping lacks a sound physical basis and can only be used in a narrow frequency band when modeling frequency-independent Q. The anelasticity, which causes the intrinsic attenuation of the material, however, can be alternatively incorporated into time domain wave-field simulations by the memory-variable technique (Day and Minster, 1984; Emmerich and Korn, 1987; Carcione *et al.*, 1988). This powerful technique can accurately model both a frequency-independent and frequency-dependent Q over a wide frequency range by using a linear combination of multiple relaxation mechanisms (e.g., Liu *et al.*, 1976). Each relaxation mechanism is represented by a set of memory variables that can be updated using first-order differential equations. The accuracy of modeling Q depends on the number of relaxation mechanisms used. More relaxation mechanisms will result in a more accurate modeling of Q. However, a large cost is associated with updating and storing the memory variables even when using just two relaxation mechanisms, which severely limits its use in 3D simulation of anelastic wave propagations (e.g., Robertsson *et al.*, 1994; Xu and McMechan, 1998).

To avoid the large cost increase associated with updating and storing the additional memory variables in 3D ap-

plications, Day (1998) and Day and Bradley (2001) developed a coarse-graining methodology for memory-variable calculations in a staggered-grid velocity-stress finite-difference scheme. In their implementation, individual relaxation mechanisms are distributed in a spatially periodic manner across adjacent finite-difference grids. For 3D models, up to eight discrete relaxation mechanisms (one per grid) can be accommodated in each coarse-grain cell. The combined effects of different relaxation mechanisms across neighboring grids can generate a good approximation of Q in the coarse-grain volume. Because only one relaxation mechanism is needed at each grid location, there is a tremendous reduction in storage and computational cost, making it practical to incorporate attenuation accurately in large-scale wave-propagation simulations. This approach has been extended by Graves and Day (2003) and Liu and Archuleta (2006).

In this article, we extend the coarse-grain approach to the explicit finite-element method. Eight pairs of relaxation times and weights are distributed in a spatially periodic manner to the center of elements where stresses are defined in the one-point integration scheme, so that each element represents a single relaxation mechanism. The stress changes caused by anelastic material response are calculated from elastic strains in the element and added to the elastic stresses. The forces caused by the total stress are then redistributed to the nodes of the element. We implement this approach in both a structured mesh and a widely used slightly unstructured mesh (see Fig. 7). The unstructured part of the mesh is only used in the vertical velocity transition zones, which allows the change of mesh densities between different velocity regions so that the number of nodes per wavelength is roughly constant everywhere.

In the following sections, we first briefly summarize the basic steps in the explicit finite-element method with the one-point integration and hourglass-control scheme. Next, we show that the one-point integration leads to an easy extension of the velocity-stress implementation of PML to the finite-element method. We demonstrate the accuracy and efficiency of PML by solving Lamb's problem and wave propagation in a layered media due to a point source. Next we show the finite-element implementation of the coarse-grain modeling of Q. We test our implementation by modeling anelastic wave propagations in a layered velocity structure with very small Qs.

Explicit Finite-Element Algorithm

For an eight-node hexahedral isoparametric element, the trilinear shape function is given in the reference plane by

$$N_I = \frac{1}{8}(1 + \xi_I\xi)(1 + \eta_I\eta)(1 + \zeta_I\zeta),$$

where (ξ, η, ζ) is the coordinate of an arbitrary point within the element in the reference plane and (ξ_I, η_I, ζ_I) is the coordinate of node I. The range of the upper-case subscripts is $\{1, 2, 3, 4, 5, 6, 7, 8\}$. The transformation between the reference plane and the physical plane is given by

$$x = x_I N_I,$$

$$y = y_I N_I,$$

and

$$z = z_I N_I,$$

where (x, y, z) is the coordinate of an arbitrary point within

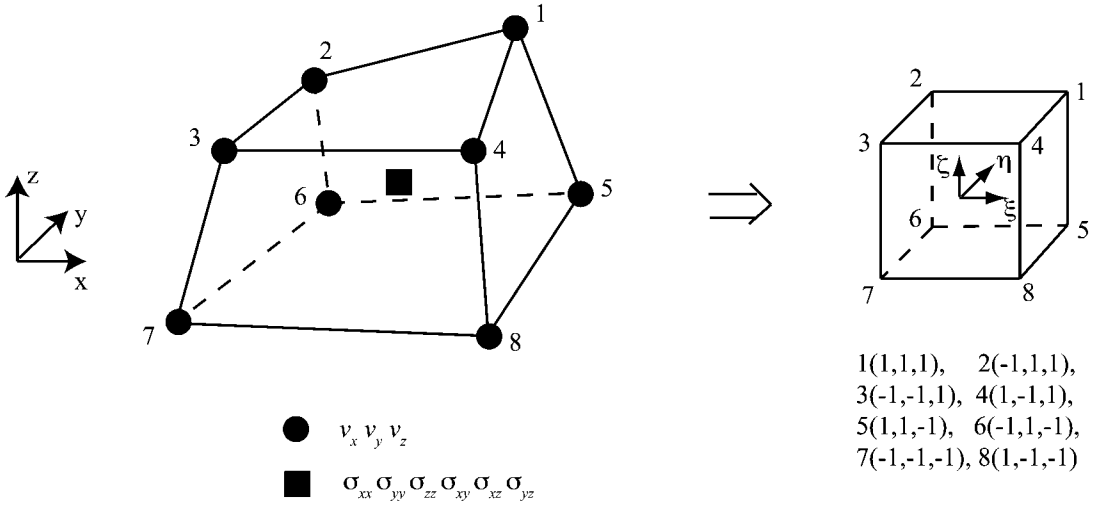

Figure 1. A hexahedreal element with arbitrary shape is transformed into a uniform cube in the reference plane through the isoparametric transformation. In the one-point integration finite-element scheme, all three components of velocity are defined at the nodes and six components of stress are defined at the element center.

the element in the physical plane and (x_I, y_I, z_I) is the coordinate of node I (Fig. 1). Summation over repeated indices is assumed. The velocity field within the element is expressed using the same shape functions as

$$v_i = v_{iI} N_I,$$

where v_{iI} is the nodal velocity. The range of lower case subscripts is $\{1, 2, 3\}$. In the one-point integration finite-element scheme, the velocities are located at the element nodes and the stresses are all defined at the center of the element (Fig. 1).

If we define

$$B_{iI} = N_{I,i}\,|_{\xi=\eta=\zeta=0}, \tag{1}$$

where the comma denotes differentiation, then the velocity gradient at the element center is

$$v_{i,j} = v_{iI} B_{jI}. \tag{2}$$

From equation (1), it can be shown that the B matrix has the following antisymmetry properties:

$$B_{j1} = -B_{j7}, \quad B_{j2} = -B_{j8}, \quad B_{j3} = -B_{j5}, \quad \text{and} \quad B_{j4} = -B_{j6}. \tag{3}$$

The detailed derivation of the B matrix is shown in Appendix A. The B matrix provides an easy way to evaluate the velocity gradient. For example, we expand $v_{x,x}$ as follows:

$$\begin{aligned} v_{x,x} &= B_{11}v_{x1} + B_{12}v_{x2} + B_{13}v_{x3} + B_{14}v_{x4} + B_{15}v_{x5} \\ &\quad + B_{16}v_{x6} + B_{17}v_{x7} + B_{18}v_{x8} \\ &= B_{11}(v_{x1} - v_{x7}) + B_{12}(v_{x2} - v_{x8}) \\ &\quad + B_{13}(v_{x3} - v_{x5}) + B_{14}(v_{x4} - v_{x6}). \end{aligned}$$

The B matrix depends only on the element geometry. For a regular element with element size h_x, h_y, and h_z along x, y, and z, respectively, the B matrix is much simplified and the preceding equation reduces to

$$v_{x,x} = \frac{1}{4h_x}(v_{x1} - v_{x2} - v_{x3} + v_{x4} + v_{x5} - v_{x6} - v_{x7} + v_{x8}),$$

which is essentially an averaged central finite-difference formula.

Calculating the element stress rate at the element center from the velocity gradient gives

$$\dot{\sigma}_{ij} = \lambda\delta_{ij}v_{l,l} + \mu(v_{i,j} + v_{j,i}), \tag{4}$$

where λ and μ are Lame's constants of the element and δ_{ij} is the Kronecker delta. The nodal force rate caused by the stress rate within the element is then given by

$$\dot{f}_{iI}^{\text{stress}} = VB_{jI}\dot{\sigma}_{ij}, \tag{5}$$

where V is the element volume. Only one Gaussian point (the center of element) has been used in the element integration. Note the use of the B matrix in the evaluation of stress divergences. For clarity, we expand the elemental nodal force rates in the y direction:

$$\begin{aligned} \dot{f}_{y1}^{\text{stress}} &= V[B_{11}\dot{\sigma}_{xy} + B_{21}\dot{\sigma}_{yy} + B_{31}\dot{\sigma}_{yz}], \\ \dot{f}_{y2}^{\text{stress}} &= V[B_{12}\dot{\sigma}_{xy} + B_{22}\dot{\sigma}_{yy} + B_{32}\dot{\sigma}_{yz}], \\ \dot{f}_{y3}^{\text{stress}} &= V[B_{13}\dot{\sigma}_{xy} + B_{23}\dot{\sigma}_{yy} + B_{33}\dot{\sigma}_{yz}], \\ \dot{f}_{y4}^{\text{stress}} &= V[B_{14}\dot{\sigma}_{xy} + B_{24}\dot{\sigma}_{yy} + B_{34}\dot{\sigma}_{yz}], \\ \dot{f}_{y5}^{\text{stress}} &= -\dot{f}_{y3}^{\text{stress}}, \dot{f}_{y6}^{\text{stress}} = -\dot{f}_{y4}^{\text{stress}}, \\ \dot{f}_{y7}^{\text{stress}} &= -\dot{f}_{y1}^{\text{stress}}, \quad \text{and} \quad \dot{f}_{y8}^{\text{stress}} = -\dot{f}_{y2}^{\text{stress}}. \end{aligned}$$

Here the antisymmetry of the B matrix has been used.

The use of one-point integration can result in certain deformation modes remaining stressless. These zero-energy modes are called hourglass modes. If a mesh is consistent with a global pattern of hourglass modes, they quickly dominate and destroy the solution. In general, both a viscous and stiffness hourglass control scheme can be used to prevent the hourglass modes from developing in the mesh (Flanagan and Belytschko, 1981).

The amplitudes of the hourglass modes in the element are given by

$$\dot{q}_{i\alpha} = v_{iI}\,\varphi_{\alpha I}, \tag{6}$$

where Greek subscripts have a range of $\{1, 2, 3, 4\}$ and the hourglass base vector φ_α is defined as follows:

$$\begin{aligned} \varphi_1 &= [1\ 1\ -1\ -1\ -1\ -1\ 1\ 1], \\ \varphi_2 &= [1\ -1\ -1\ 1\ -1\ 1\ 1\ -1], \\ \varphi_3 &= [1\ -1\ 1\ -1\ 1\ -1\ 1\ -1], \end{aligned}$$

and

$$\varphi_4 = [-1\ 1\ -1\ 1\ 1\ -1\ 1\ -1].$$

In a viscous hourglass control scheme, the hourglass forces can be approximated by

$$f_{iI}^{vhg} = \chi\rho V_p V^{2/3}\dot{q}_{i\alpha}\varphi_{\alpha I}, \tag{7}$$

where ρ and V_P are the density and the P-wave velocity of the element, respectively, and χ is a tunable parameter that is usually set in the range 0.05–0.15 (Goudreau and Hallquist, 1982).

If a stiffness hourglass control scheme is used, the stiffness hourglass force rates can be approximated by

$$\dot{f}_{iI}^{ehg} = \frac{\kappa}{16}(\lambda + 2\mu)V^{1/3}\dot{q}_{i\alpha}\varphi_{\alpha I}, \tag{8}$$

where the tunable parameter κ is usually 0.3. The rate form is used for the stiffness hourglass control because it is more suitable for large deformation problems (Flanagan and Belytschko, 1981). The total elastic nodal force rate caused by both the stress and hourglass modes is given by

$$\dot{f}_{jI}^{\text{elastic}} = \dot{f}_{jI}^{\text{stress}} + \dot{f}_{jI}^{ehg}. \tag{9}$$

In the viscous hourglass approach, the hourglass modes are effectively damped by the hourglass forces. Some hourglassing may, however, still occur. Because there is no stiffness in the hourglass control, mesh distortion caused by small hourglassing is permanent. The viscous and stiffness hourglass control schemes can, however, be used together to eliminate the permanent mesh distortion. The advantage of the viscous hourglass damping is that it is orthogonal to the uniform strain mode for a parallelpiped element, that is, the solution is insensitive to the level of the damping. Thus, it provides an effective way to kill the spurious high-frequency oscillations during the calculation. For example, the viscous hourglass damping can be applied in the simulation of earthquake-rupture dynamics (Day, 1982; Day *et al.*, 2005) to provide a "clean" slip-rate field, where large oscillations can affect the rupture speed.

Flanagan and Belytschko (1981) present a slightly different hourglass control formulation, where the hourglass forces are orthogonal to the uniform strain mode for any element shape. Belytschko *et al.* (1984) point out that the hourglass forces in the preceding scheme can affect the uniform strain mode for nonparallelpiped elements, and therefore does not exactly meet the consistency conditions. The effects of the small deviation from consistency are, however, not yet known. Goudreau and Hallquist (1982) demonstrate that this scheme works satisfactorily for most cases. For its simplicity and efficiency, this formulation has become the core of many commercial finite-element software programs. We use this formulation in the remainder of this article. The formulation of Flanagan and Belytschko (1981) can be similarly implemented.

The detailed computational sequence for the implementation of one-point integration with the hourglass control schemes is shown in Appendix B. Because second-order hexahedral elements are used exclusively in the mesh, the mass matrix can be easily lumped into a diagonal matrix, thus leading to a highly efficient explicit finite-element scheme. It requires a minimum of 10 nodes per wavelength. The stability condition is given by $\Delta t < h^{eq}/V_P$, where Δt is the timestep and h^{eq} is the equivalent element size.

Modeling of PML

Formulation

In the typical PML formulation, each velocity or stress component is split into two additional components: one is normal to the PML-interior interface and the other is parallel with the interface, with the damping associated only with the normal component. Such split and selectively damped elastodynamic equations lead to a nonreflective PML-interior interface before spatial discretization with the waves decaying exponentially in the PML. After the PML is discretized in numerical methods, the PML-interior interface is no longer nonreflective due to numerical dispersion and a finite layer width. However, the reflection can be kept sufficiently small even with a very thin layer width and a smooth damping profile.

Following Collino and Tsogka (2001), the three-dimensional equations of motion in the PML region can be split into

$$\begin{aligned}
&v_x = {}^{x}v_x + {}^{y}v_x + {}^{z}v_x,\\
&\rho[{}^{x}v_{x,t} + d(x^{v})\,{}^{x}v_x] = \sigma_{xx,x},\\
&\rho[{}^{y}v_{x,t} + d(y^{v})\,{}^{y}v_x] = \sigma_{xy,y},\\
&\rho[{}^{z}v_{x,t} + d(z^{v})\,{}^{z}v_x] = \sigma_{xz,z},\\
&v_y = {}^{x}v_y + {}^{y}v_y + {}^{z}v_y,\\
&\rho[{}^{x}v_{y,t} + d(x^{v})\,{}^{x}v_y] = \sigma_{xy,x},\\
&\rho[{}^{y}v_{y,t} + d(y^{v})\,{}^{y}v_y] = \sigma_{yy,y},\\
&\rho[{}^{z}v_{y,t} + d(z^{v})\,{}^{z}v_y] = \sigma_{yz,z},\\
&v_z = {}^{x}v_z + {}^{y}v_z + {}^{z}v_z,\\
&\rho[{}^{x}v_{z,t} + d(x^{v})\,{}^{x}v_z] = \sigma_{xz,x},\\
&\rho[{}^{y}v_{z,t} + d(y^{v})\,{}^{y}v_z] = \sigma_{yz,y},\\
&\rho[{}^{z}v_{z,t} + d(z^{v})\,{}^{z}v_z] = \sigma_{zz,z},
\end{aligned} \tag{10}$$

and the Hooke's Law can be similarly given by

$$\begin{aligned}
&\sigma_{xx} = {}^{x}\sigma_{xx} + {}^{y}\sigma_{xx} + {}^{z}\sigma_{xx},\\
&{}^{x}\sigma_{xx,t} + d(x^{\sigma})\,{}^{x}\sigma_{xx} = (\lambda + 2\mu)v_{x,x},\\
&{}^{y}\sigma_{xx,t} + d(y^{\sigma})\,{}^{y}\sigma_{xx} = \lambda v_{y,y},\\
&{}^{z}\sigma_{xx,t} + d(z^{\sigma})\,{}^{z}\sigma_{xx} = \lambda v_{z,z},\\
&\sigma_{yy} = {}^{x}\sigma_{yy} + {}^{y}\sigma_{yy} + {}^{z}\sigma_{yy},\\
&{}^{x}\sigma_{yy,t} + d(x^{\sigma})\,{}^{x}\sigma_{yy} = \lambda v_{x,x},\\
&{}^{y}\sigma_{yy,t} + d(y^{\sigma})\,{}^{y}\sigma_{yy} = (\lambda + 2\mu)v_{y,y},\\
&{}^{z}\sigma_{yy,t} + d(z^{\sigma})\,{}^{z}\sigma_{yy} = \lambda v_{z,z},\\
&\sigma_{zz} = {}^{x}\sigma_{zz} + {}^{y}\sigma_{zz} + {}^{z}\sigma_{zz},\\
&{}^{x}\sigma_{zz,t} + d(x^{\sigma})\,{}^{x}\sigma_{zz} = \lambda v_{x,x},\\
&{}^{y}\sigma_{zz,t} + d(y^{\sigma})\,{}^{y}\sigma_{zz} = \lambda v_{y,y},\\
&{}^{z}\sigma_{zz,t} + d(z^{\sigma})\,{}^{z}\sigma_{zz} = (\lambda + 2\mu)v_{z,z},
\end{aligned} \tag{11}$$

$$
\begin{aligned}
\sigma_{xy} &= {}^{x}\sigma_{xy} + {}^{y}\sigma_{xy},\\
{}^{x}\sigma_{xy,t} &+ d(x^{\sigma})\,{}^{x}\sigma_{xy} = \mu v_{y,x},\\
{}^{y}\sigma_{xy,t} &+ d(y^{\sigma})\,{}^{y}\sigma_{xy} = \mu v_{x,y},\\
\sigma_{xz} &= {}^{x}\sigma_{xz} + {}^{z}\sigma_{xz},\\
{}^{x}\sigma_{xz,t} &+ d(x^{\sigma})\,{}^{x}\sigma_{xz} = \mu v_{z,x},\\
{}^{z}\sigma_{xz,t} &+ d(z^{\sigma})\,{}^{z}\sigma_{xz} = \mu v_{x,z},\\
\sigma_{yz} &= {}^{y}\sigma_{yz} + {}^{z}\sigma_{yz},\\
{}^{y}\sigma_{yz,t} &+ d(y^{\sigma})\,{}^{y}\sigma_{yz} = \mu v_{z,y},\\
{}^{z}\sigma_{yz,t} &+ d(z^{\sigma})\,{}^{z}\sigma_{yz} = \mu v_{y,z},
\end{aligned}
$$

where d is the damping profile, x^{v}, y^{v}, and z^{v} are the distances from an element node where the velocity is defined to the PML-interior interface along x, y, and z, respectively, and x^{σ}, y^{σ}, and z^{σ} are the distances measured from the center of an element where the stress is defined to the interface. Equations (10) and (11) are given for the general case. Note that the damping terms in the equations can be zero depending on the element location in the PML region. If an element is in the PML-bounding plane, then there is only one nonzero damping term. For elements in edge regions, damping takes effect in two directions; therefore, only one damping term is zero. For elements in corner regions, all three damping terms are nonzero. We refer the reader to figure 2 in Marcinkovich and Olsen (2003) for more details on the geometry.

After discretizing the PML region using eight-node hexahedral elements, the discrete form of the preceding equations can be easily obtained following the one-point integration scheme shown previously.

The velocity gradient can be obtained from the B matrix by using:

$$
\begin{aligned}
D_x v_i &= B_{11}(v_{i1}^{n-1/2} - v_{i7}^{n-1/2}) + B_{12}(v_{i2}^{n-1/2} - v_{i8}^{n-1/2})\\
&\quad + B_{13}(v_{i3}^{n-1/2} - v_{i5}^{n-1/2}) + B_{14}(v_{i4}^{n-1/2} - v_{i6}^{n-1/2}),\\
D_y v_i &= B_{21}(v_{i1}^{n-1/2} - v_{i7}^{n-1/2}) + B_{22}(v_{i2}^{n-1/2} - v_{i8}^{n-1/2})\\
&\quad + B_{23}(v_{i3}^{n-1/2} - v_{i5}^{n-1/2}) + B_{24}(v_{i4}^{n-1/2} - v_{i6}^{n-1/2}),\\
D_z v_i &= B_{31}(v_{i1}^{n-1/2} - v_{i7}^{n-1/2}) + B_{32}(v_{i2}^{n-1/2} - v_{i8}^{n-1/2})\\
&\quad + B_{33}(v_{i3}^{n-1/2} - v_{i5}^{n-1/2}) + B_{34}(v_{i4}^{n-1/2} - v_{i6}^{n-1/2}),
\end{aligned}
$$

where n is the temporal index. Then the discrete form of equation (11) follows straightforwardly:

$$
\begin{aligned}
\sigma_{xx}^{n} &= {}^{x}\sigma_{xx}^{n} + {}^{y}\sigma_{xx}^{n} + {}^{z}\sigma_{xx}^{n},\\
\frac{{}^{x}\sigma_{xx}^{n} - {}^{x}\sigma_{xx}^{n-1}}{\Delta t} &+ d(x^{\sigma})\,\frac{{}^{x}\sigma_{xx}^{n} + {}^{x}\sigma_{xx}^{n-1}}{2} = (\lambda + 2\mu) D_x v_x,\\
\frac{{}^{y}\sigma_{xx}^{n} - {}^{y}\sigma_{xx}^{n-1}}{\Delta t} &+ d(y^{\sigma})\,\frac{{}^{y}\sigma_{xx}^{n} + {}^{y}\sigma_{xx}^{n-1}}{2} = \lambda D_y v_y,\\
\frac{{}^{z}\sigma_{xx}^{n} - {}^{z}\sigma_{xx}^{n-1}}{\Delta t} &+ d(z^{\sigma})\,\frac{{}^{z}\sigma_{xx}^{n} + {}^{z}\sigma_{xx}^{n-1}}{2} = \lambda D_z v_z,\\
\sigma_{yy}^{n} &= {}^{x}\sigma_{yy}^{n} + {}^{y}\sigma_{yy}^{n} + {}^{z}\sigma_{yy}^{n},\\
\frac{{}^{x}\sigma_{yy}^{n} - {}^{x}\sigma_{yy}^{n-1}}{\Delta t} &+ d(x^{\sigma})\,\frac{{}^{x}\sigma_{yy}^{n} + {}^{x}\sigma_{yy}^{n-1}}{2} = \lambda D_x v_x,\\
\frac{{}^{y}\sigma_{yy}^{n} - {}^{y}\sigma_{yy}^{n-1}}{\Delta t} &+ d(y^{\sigma})\,\frac{{}^{y}\sigma_{yy}^{n} + {}^{y}\sigma_{yy}^{n-1}}{2} = (\lambda + 2\mu) D_y v_y,\\
\frac{{}^{z}\sigma_{yy}^{n} - {}^{z}\sigma_{yy}^{n-1}}{\Delta t} &+ d(z^{\sigma})\,\frac{{}^{z}\sigma_{yy}^{n} + {}^{z}\sigma_{yy}^{n-1}}{2} = \lambda D_z v_z,\\
\sigma_{zz}^{n} &= {}^{x}\sigma_{zz}^{n} + {}^{y}\sigma_{zz}^{n} + {}^{z}\sigma_{zz}^{n},\\
\frac{{}^{x}\sigma_{zz}^{n} - {}^{x}\sigma_{zz}^{n-1}}{\Delta t} &+ d(x^{\sigma})\,\frac{{}^{x}\sigma_{zz}^{n} + {}^{x}\sigma_{zz}^{n-1}}{2} = \lambda D_x v_x,\\
\frac{{}^{y}\sigma_{zz}^{n} - {}^{y}\sigma_{zz}^{n-1}}{\Delta t} &+ d(y^{\sigma})\,\frac{{}^{y}\sigma_{zz}^{n} + {}^{y}\sigma_{zz}^{n-1}}{2} = \lambda D_y v_y,\\
\frac{{}^{z}\sigma_{zz}^{n} - {}^{z}\sigma_{zz}^{n-1}}{\Delta t} &+ d(z^{\sigma})\,\frac{{}^{z}\sigma_{zz}^{n} + {}^{z}\sigma_{zz}^{n-1}}{2} = (\lambda + 2\mu) D_z v_z,\\
\sigma_{xy}^{n} &= {}^{x}\sigma_{xy}^{n} + {}^{y}\sigma_{xy}^{n},\\
\frac{{}^{x}\sigma_{xy}^{n} - {}^{x}\sigma_{xy}^{n-1}}{\Delta t} &+ d(x^{\sigma})\,\frac{{}^{x}\sigma_{xy}^{n} + {}^{x}\sigma_{xy}^{n-1}}{2} = \mu D_x v_y,\\
\frac{{}^{y}\sigma_{xy}^{n} - {}^{y}\sigma_{xy}^{n-1}}{\Delta t} &+ d(y^{\sigma})\,\frac{{}^{y}\sigma_{xy}^{n} + {}^{y}\sigma_{xy}^{n-1}}{2} = \mu D_y v_x,\\
\sigma_{xz}^{n} &= {}^{x}\sigma_{xz}^{n} + {}^{z}\sigma_{xz}^{n},\\
\frac{{}^{x}\sigma_{xz}^{n} - {}^{x}\sigma_{xz}^{n-1}}{\Delta t} &+ d(x^{\sigma})\,\frac{{}^{x}\sigma_{xz}^{n} + {}^{x}\sigma_{xz}^{n-1}}{2} = \mu D_x v_z,\\
\frac{{}^{z}\sigma_{xz}^{n} - {}^{z}\sigma_{xz}^{n-1}}{\Delta t} &+ d(z^{\sigma})\,\frac{{}^{z}\sigma_{xz}^{n} + {}^{z}\sigma_{xz}^{n-1}}{2} = \mu D_z v_x,\\
\sigma_{yz}^{n} &= {}^{y}\sigma_{yz}^{n} + {}^{z}\sigma_{yz}^{n},\\
\frac{{}^{y}\sigma_{yz}^{n} - {}^{y}\sigma_{yz}^{n-1}}{\Delta t} &+ d(y^{\sigma})\,\frac{{}^{y}\sigma_{yz}^{n} + {}^{y}\sigma_{yz}^{n-1}}{2} = \mu D_y v_z,\\
\frac{{}^{z}\sigma_{yz}^{n} - {}^{z}\sigma_{yz}^{n-1}}{\Delta t} &+ d(z^{\sigma})\,\frac{{}^{z}\sigma_{yz}^{n} + {}^{z}\sigma_{yz}^{n-1}}{2} = \mu D_z v_y.
\end{aligned}
\tag{12}
$$

To discretize equation (10), we take two steps. First, we use the B matrix to calculate the elemental nodal forces caused by the stress derivatives on the right side of equation (10):

Elemental nodal forces along x

$$
\begin{aligned}
{}^{x}f^{e}_{x1} &= VB_{11}\sigma^{n}_{xx},\ {}^{y}f^{e}_{x1} = VB_{21}\sigma^{n}_{xy},\ {}^{z}f^{e}_{x1} = VB_{31}\sigma^{n}_{xz},\\
{}^{x}f^{e}_{x2} &= VB_{12}\sigma^{n}_{xx},\ {}^{y}f^{e}_{x2} = VB_{22}\sigma^{n}_{xy},\ {}^{z}f^{e}_{x2} = VB_{32}\sigma^{n}_{xz},\\
{}^{x}f^{e}_{x3} &= VB_{13}\sigma^{n}_{xx},\ {}^{y}f^{e}_{x3} = VB_{23}\sigma^{n}_{xy},\ {}^{z}f^{e}_{x3} = VB_{33}\sigma^{n}_{xz},\\
{}^{x}f^{e}_{x4} &= VB_{14}\sigma^{n}_{xx},\ {}^{y}f^{e}_{x4} = VB_{24}\sigma^{n}_{xy},\ {}^{z}f^{e}_{x4} = VB_{34}\sigma^{n}_{xz},\\
{}^{x}f^{e}_{x5} &= -{}^{x}f^{e}_{x3},\ {}^{y}f^{e}_{x5} = -{}^{y}f^{e}_{x3},\ {}^{z}f^{e}_{x5} = -{}^{z}f^{e}_{x3},\\
{}^{x}f^{e}_{x6} &= -{}^{x}f^{e}_{x4},\ {}^{y}f^{e}_{x6} = -{}^{y}f^{e}_{x4},\ {}^{z}f^{e}_{x6} = -{}^{z}f^{e}_{x4},\\
{}^{x}f^{e}_{x7} &= -{}^{x}f^{e}_{x1},\ {}^{y}f^{e}_{x7} = -{}^{y}f^{e}_{x1},\ {}^{z}f^{e}_{x7} = -{}^{z}f^{e}_{x1},\\
{}^{x}f^{e}_{x8} &= -{}^{x}f^{e}_{x2},\ {}^{y}f^{e}_{x8} = -{}^{y}f^{e}_{x2},\ {}^{z}f^{e}_{x8} = -{}^{z}f^{e}_{x2},
\end{aligned}
$$

Elemental nodal forces along y

$$
\begin{aligned}
{}^{x}f^{e}_{y1} &= VB_{11}\sigma^{n}_{xy},\ {}^{y}f^{e}_{y1} = VB_{21}\sigma^{n}_{yy},\ {}^{z}f^{e}_{y1} = VB_{31}\sigma^{n}_{yz},\\
{}^{x}f^{e}_{y2} &= VB_{12}\sigma^{n}_{xy},\ {}^{y}f^{e}_{y2} = VB_{22}\sigma^{n}_{yy},\ {}^{z}f^{e}_{y2} = VB_{32}\sigma^{n}_{yz},\\
{}^{x}f^{e}_{y3} &= VB_{13}\sigma^{n}_{xy},\ {}^{y}f^{e}_{y3} = VB_{23}\sigma^{n}_{yy},\ {}^{z}f^{e}_{y3} = VB_{33}\sigma^{n}_{yz},\\
{}^{x}f^{e}_{y4} &= VB_{14}\sigma^{n}_{xy},\ {}^{y}f^{e}_{y4} = VB_{24}\sigma^{n}_{yy},\ {}^{z}f^{e}_{y4} = VB_{34}\sigma^{n}_{yz},\\
{}^{x}f^{e}_{y5} &= -{}^{x}f^{e}_{y3},\ {}^{y}f^{e}_{y5} = -{}^{y}f^{e}_{y3},\ {}^{z}f^{e}_{y5} = -{}^{z}f^{e}_{y3},\\
{}^{x}f^{e}_{y6} &= -{}^{x}f^{e}_{y4},\ {}^{y}f^{e}_{y6} = -{}^{y}f^{e}_{y4},\ {}^{z}f^{e}_{y6} = -{}^{z}f^{e}_{y4},\\
{}^{x}f^{e}_{y7} &= -{}^{x}f^{e}_{y1},\ {}^{y}f^{e}_{y7} = -{}^{y}f^{e}_{y1},\ {}^{z}f^{e}_{y7} = -{}^{z}f^{e}_{y1},\\
{}^{x}f^{e}_{y8} &= -{}^{x}f^{e}_{y2},\ {}^{y}f^{e}_{y8} = -{}^{y}f^{e}_{y2},\ {}^{z}f^{e}_{y8} = -{}^{z}f^{e}_{y2},
\end{aligned}
$$

Elemental nodal forces along z

$$
\begin{aligned}
{}^{x}f^{e}_{z1} &= VB_{11}\sigma^{n}_{xz},\ {}^{y}f^{e}_{z1} = VB_{21}\sigma^{n}_{yz},\ {}^{z}f^{e}_{z1},\ = VB_{31}\sigma^{n}_{zz},\\
{}^{x}f^{e}_{z2} &= VB_{12}\sigma^{n}_{xz},\ {}^{y}f^{e}_{z2} = VB_{22}\sigma^{n}_{yz},\ {}^{z}f^{e}_{z2} = VB_{32}\sigma^{n}_{zz},\\
{}^{x}f^{e}_{z3} &= VB_{13}\sigma^{n}_{xz},\ {}^{y}f^{e}_{z3} = VB_{23}\sigma^{n}_{yz},\ {}^{z}f^{e}_{z3} = VB_{33}\sigma^{n}_{zz},\\
{}^{x}f^{e}_{z4} &= VB_{14}\sigma^{n}_{xz},\ {}^{y}f^{e}_{z4} = VB_{24}\sigma^{n}_{yz},\ {}^{z}f^{e}_{z4} = VB_{34}\sigma^{n}_{zz},\\
{}^{x}f^{e}_{z5} &= -{}^{x}f^{e}_{z3},\ {}^{y}f^{e}_{z5} = -{}^{y}f^{e}_{z3},\ {}^{z}f^{e}_{z5} = -{}^{z}f^{e}_{z3},\\
{}^{x}f^{e}_{z6} &= -{}^{x}f^{e}_{z4},\ {}^{y}f^{e}_{z6} = -{}^{y}f^{e}_{z4},\ {}^{z}f^{e}_{z6} = -{}^{z}f^{e}_{z4},\\
{}^{x}f^{e}_{z7} &= -{}^{x}f^{e}_{z1},\ {}^{y}f^{e}_{z7} = -{}^{y}f^{e}_{z1},\ {}^{z}f^{e}_{z7} = -{}^{z}f^{e}_{z1}.\\
{}^{x}f^{e}_{z8} &= -{}^{x}f^{e}_{z2},\ {}^{y}f^{e}_{z8} = -{}^{y}f^{e}_{z2},\ {}^{z}f^{e}_{z8} = -{}^{z}f^{e}_{z2}.
\end{aligned}
$$

Then the discrete form of the equation (10) is given by

$$
\begin{aligned}
M\left(\frac{{}^{x}V_i^{n+1/2} - {}^{x}V_i^{n-1/2}}{\Delta t} + D(x^{v})\,\frac{{}^{x}V_i^{n+1/2} + {}^{x}V_i^{n-1/2}}{2}\right) &= -\sum_e {}^{x}f_i^{e},\\
M\left(\frac{{}^{y}V_i^{n+1/2} - {}^{y}V_i^{n-1/2}}{\Delta t} + D(y^{v})\,\frac{{}^{y}V_i^{n+1/2} + {}^{y}V_i^{n-1/2}}{2}\right) &= -\sum_e {}^{y}f_i^{e}, \qquad (14)\\
M\left(\frac{{}^{z}V_i^{n+1/2} - {}^{z}V_i^{n-1/2}}{\Delta t} + D(z^{v})\,\frac{{}^{z}V_i^{n+1/2} + {}^{z}V_i^{n-1/2}}{2}\right) &= -\sum_e {}^{z}f_i^{e},
\end{aligned}
$$

where M is the global mass vector, i is the direction x, y, or z, ${}^{x}V_i$, ${}^{y}V_i$, and ${}^{z}V_i$ are the three global velocity vectors, D is the global vector associated with damping, and $\sum_e {}^{x}f_i^{e}$, $\sum_e {}^{y}f_i^{e}$, and $\sum_e {}^{z}f_i^{e}$ represent the global internal force vectors assembled by summing the elemental nodal force contributions from all the elements in the PML region. In this discretization, however, hourglass modes can develop in the PML region.

To control the hourglass modes, we introduce a new velocity component: the hourglass velocity ${}^{hg}v_i$, which is only associated with the hourglass forces. We tested both the viscous and stiffness hourglass control schemes in the PML and found that the PML becomes unstable with the use of a stiffness hourglass scheme. Therefore, we use only the viscous hourglass control in the PML. Following equation (7), the viscous hourglass force caused by nodal velocity is given by

$$
\begin{aligned}
{}^{hg}f^{e}_{i1} &= \chi\rho V_P V^{2/3}(b_i + c_i + d_i - e_i),\\
{}^{hg}f^{e}_{i2} &= \chi\rho V_P V^{2/3}(b_i - c_i - d_i + e_i),\\
{}^{hg}f^{e}_{i3} &= \chi\rho V_P V^{2/3}(-b_i - c_i + d_i - e_i),\\
{}^{hg}f^{e}_{i4} &= \chi\rho V_P V^{2/3}(-b_i + c_i - d_i + e_i),\\
{}^{hg}f^{e}_{i5} &= \chi\rho V_P V^{2/3}(-b_i - c_i + d_i + e_i),\\
{}^{hg}f^{e}_{i6} &= \chi\rho V_P V^{2/3}(-b_i + c_i - d_i - e_i),\\
{}^{hg}f^{e}_{i7} &= \chi\rho V_P V^{2/3}(b_i + c_i + d_i + e_i),\\
{}^{hg}f^{e}_{i8} &= \chi\rho V_P V^{2/3}(b_i - c_i - d_i - e_i),
\end{aligned}
$$

where i is the direction x, y, or z, and

$$
\begin{aligned}
b_i &= v_{i1} + v_{i2} - v_{i3} - v_{i4} - v_{i5} - v_{i6} + v_{i7} + v_{i8},\\
c_i &= v_{i1} - v_{i2} - v_{i3} + v_{i4} - v_{i5} + v_{i6} + v_{i7} - v_{i8},\\
d_i &= v_{i1} - v_{i2} + v_{i3} - v_{i4} + v_{i5} - v_{i6} + v_{i7} - v_{i8},\\
e_i &= -v_{i1} + v_{i2} - v_{i3} + v_{i4} + v_{i5} - v_{i6} + v_{i7} - v_{i8}.
\end{aligned} \qquad (15)
$$

Then the global hourglass velocity ${}^{hg}V_i$ can be simply updated by

$$
M\,\frac{{}^{hg}V_i^{n+1/2} - {}^{hg}V_i^{n-1/2}}{\Delta t} = -\sum_e {}^{hg}f_i^{e}, \qquad (16)
$$

where i is the direction x, y, or z and $\sum_e {}^{hg}f_i^e$ is the global hourglass force vector formed by summing the elemental hourglass forces over all the elements in the PML. Finally, the total velocity V_i can be updated using

$$V_i^{n+1/2} = {}^{x}V_i^{n+1/2} + {}^{y}V_i^{n+1/2} + {}^{z}V_i^{n+1/2} + {}^{hg}V_i^{n+1/2}. \quad (17)$$

At the outer boundary of the PML region, we impose Dirichlet boundary conditions, that is, we set the velocities to zero. At the interface of the PML and the interior, we impose the velocity-boundary conditions by using the velocities along the interface calculated in the interior region.

Numerical Examples

There can be different functional forms associated with the damping profile $d(x)$. In the following examples we use

$$d(x) = \frac{3V_P}{2\Delta} \log\left(\frac{1}{R}\right)\left(\frac{x}{\Delta}\right)^2, \quad (18)$$

which is used by many investigators, for example, Collino and Tsogka (2001), where Δ is the width of the PML, x is the distance perpendicular to the PML-interior interface along which the velocity or stress component normal to the interface is damped, and R is the theoretical reflection coefficient when a plane P wave is incident normal to the PML. In the following examples, we use $\Delta = 6h$, where h is the element size in the case of a uniform mesh or the largest element size in the case of the unstructured mesh shown in Figure 7, and the theoretical reflection coefficient $R = 0.01$.

Lamb's Problem. Classic ABCs absorb body waves relatively well, especially when the incident wave is normal to the boundary. They behave rather poorly for Rayleigh waves. This is largely due to the elliptical particle motions of Rayleigh waves. In Lamb's problem, a strong Rayleigh wave is excited by applying an impulselike surface load, thus providing a good test for the performance of PML in absorbing surface waves.

We apply a vertical force at the free surface of a homogeneous half-space. The geometry of the physical problem and material properties are shown in Figure 2. The dimensions of the model are 6 km × 6 km × 3 km. The force is a narrow-banded Gaussian type of pulse with a functional form $f(t) = A \exp[-1000(t - t_0)^2]$, where the amplitude $A = 10^{13}$ N, and $t_0 = 0.25$ sec. We discretize the model by using uniform cubic elements with a length of 20 m. The timestep is 3.25 msec.

We surround the model by PMLs with a thickness of 120 m, except for the free surface. We compare the solutions of the PML to the first-order absorbing boundary of Lysmer and Kuhlmeyer (1969). Simple dampers are used along the model boundary in the formulation of Lysmer and Kuhlmeyer (1969), which has about the same accuracy as the first-order paraxial approximation of Clayton and Engquist (1977).

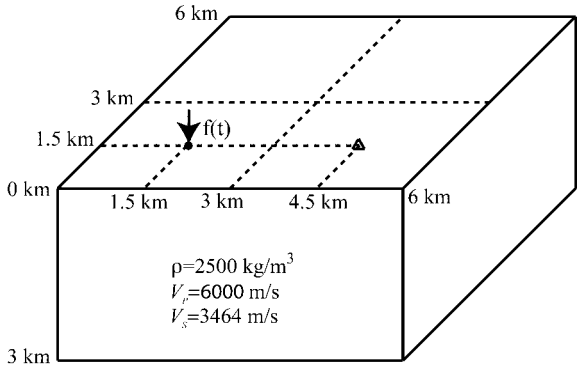

Figure 2. Model for the Lamb's problem. A vertical force is applied at the surface of a homogeneous half-space. A small triangle denotes the observation point.

Figure 3 shows snapshots of wave propagation at different instants of time. Because of the symmetry conditions, only one horizontal component of surface displacement is shown. The largest amplitude in the snapshots corresponds to the Rayleigh wavefront. Strong reflections are seen from the first-order absorbing boundaries. The reflection coefficient for this ABC is about 10%. Almost no reflections are observed from the PML when the results are presented in the normal scale. Indeed, to see the reflection from the PML clearly, we magnify the results by a factor 50 (see Fig. 4). The reflection coefficient for the PML is about 1%, very close to the theoretical reflection coefficient R that we used in equation (18). We show the displacement time histories at the observation point, 3 km from the source, in Figure 5. The direct P wave, S wave, and nondispersive Rayleigh wave can be clearly seen. Again strong reflections are observed in the first-order absorbing boundary, and almost no waves are reflected from the PML, showing an excellent absorption of Rayleigh waves with PML. The tangential displacement should be zero because of the problem's symmetry, but spurious energy is observed from the first-order absorbing boundary.

A Double-Couple Point Source. In our second example, we model a double-couple point source in a one-layered velocity structure. The geometry of the model and material properties are shown in Figure 6. The dimension of the model is 20 km × 20 km × 12 km. The double-couple source with strike, 90°; dip, 90°; rake, 0°; and M_0 10^{16} N m is located at depth 2 km, and the moment rate function is a cosine function given by

$$\dot{M}(t) = \begin{cases} \dfrac{M_0}{T}\left(1 - \cos\dfrac{2\pi t}{T}\right), & \text{if } 0 \le t \le T \\ 0, & \text{otherwise} \end{cases}$$

with a width of $T = 0.2$ sec.

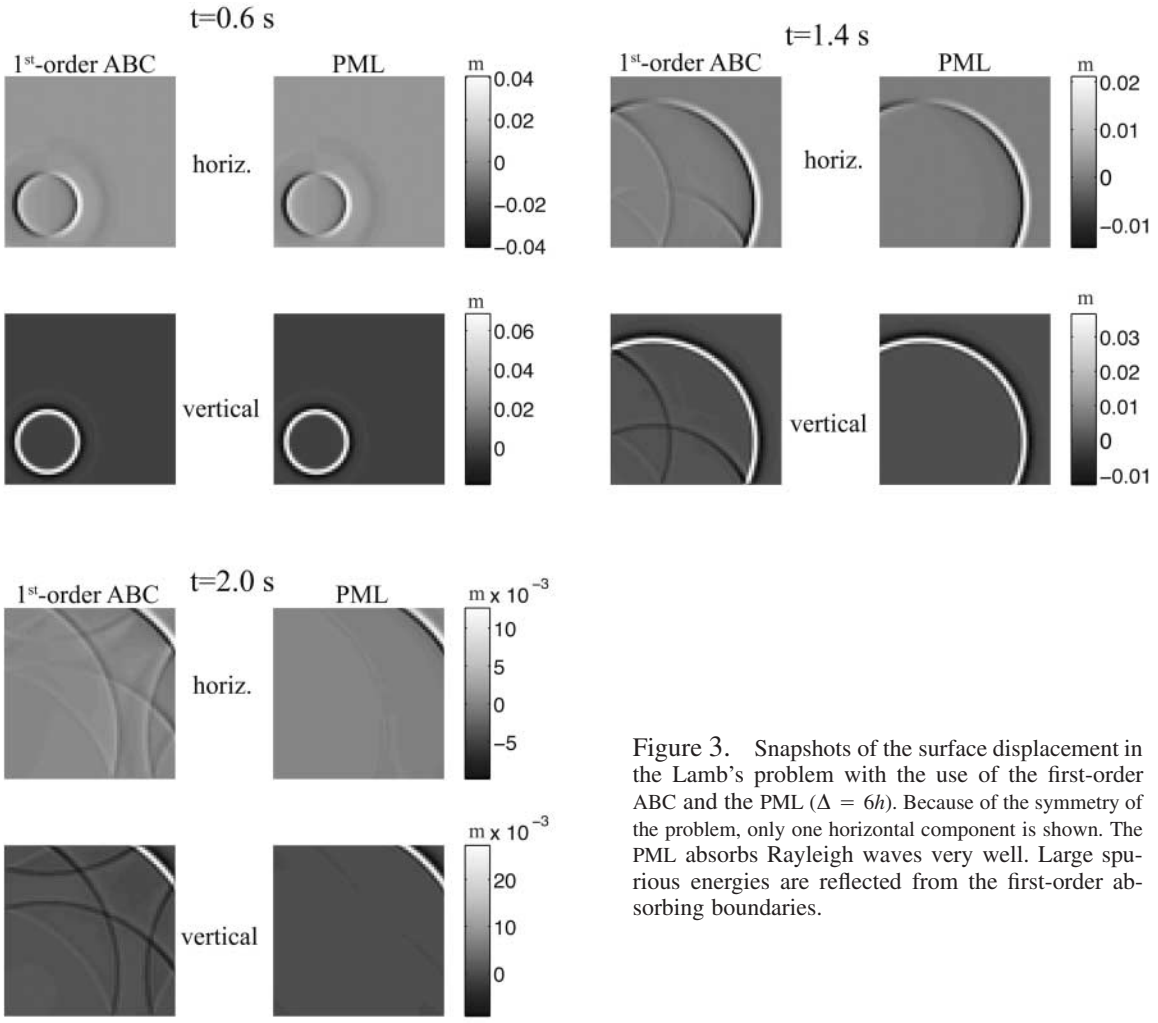

Figure 3. Snapshots of the surface displacement in the Lamb's problem with the use of the first-order ABC and the PML ($\Delta = 6h$). Because of the symmetry of the problem, only one horizontal component is shown. The PML absorbs Rayleigh waves very well. Large spurious energies are reflected from the first-order absorbing boundaries.

We use a slightly unstructured mesh (Fig. 7) to discretize the model. The advantage of the unstructured mesh shown in Figure 7 is that the mesh can be coarsened with depth to retain a similar number of nodes per wavelength. In general, seismic-wave speed increases with depth. The element sizes are first doubled in one horizontal dimension and, subsequently, at a greater depth, in the second horizontal dimension. The mesh coarsening can be made as many times as is appropriate. This implementation dramatically decreases the number of degrees of freedom without losing accuracy in wave-propagation modeling. Outside the velocity transition zones, the mesh is structured. This mesh has been widely used in the spectral-element simulation of both regional and global wave propagations (Komatitsch and Tromp, 1999, 2002a,b; Komatitsch *et al.*, 2002, 2004). In our example, we discretize the top layer and half-space with uniform elements of size of 50 m and 100 m, respectively. There is one transition zone where the element size is doubled from 50 m to 100 m starting from the layer interface and extending over four elements to 1.2 km at depth. The timestep is 8 msec. We calculate waves up to 3 Hz.

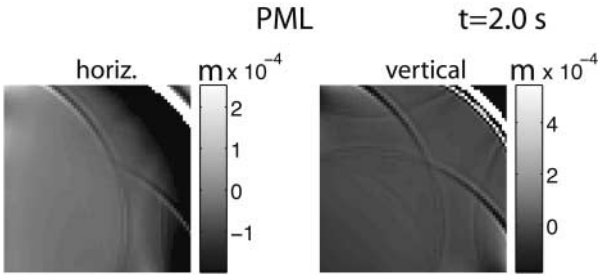

Figure 4. The snapshots with the PML ($\Delta = 6h$) at 2 sec in the Lamb's problem are magnified by a factor of 50 to see the reflections.

To implement the PML, we extend the mesh for 600 m from the interior region to the PML region, except at the free surface. Thus, the element size is also doubled from depth 1 km to 1.2 km in the PML. Outside the transition zone, the elements are uniform. Figure 8 shows snapshots of horizontal and vertical surface velocities at two instants of time. Because of the symmetry of the problem, only one horizontal component is shown. Waves with incident angle normal to

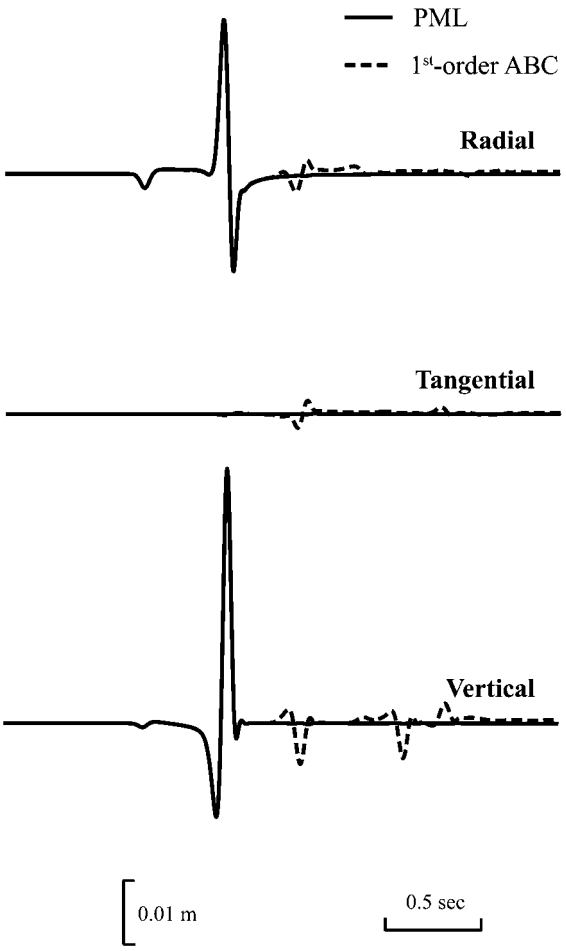

Figure 5. Comparisons of displacement time histories at the observation point for the Lamb's problem using the PML ($\Delta = 6h$) and the first-order ABC. All three components are plotted on the same scale. Because of the symmetry of the problem, the tangential component should be zero. The first-order ABC behaves rather poorly for the Rayleigh wave and large spurious waves are reflected. The PML absorbs Rayleigh waves very well without observable reflections.

the boundary are well absorbed by the first-order ABC. For other incident angles, however, the reflection is large. At 15 sec, the reflected waves dominate the solution in the interior region. An excellent absorption is obtained by PML for waves with almost all incident angles. Figure 9 compares the velocity time histories at the observation point. Strong reflections (reflection coefficient ~10%) are observed from the first-order absorbing boundary, whereas there are almost no observable reflections from the PML. To see the reflections from the PML, we magnify the time histories after 20 sec by a factor about 100 (see Fig. 9d). The reflection coefficient is about 1%. The reflections from the first-order absorbing boundary affect the time histories as early as ~3 sec. This example illustrates the good performance of the PML with strong body waves, even with irregular elements in the PML region.

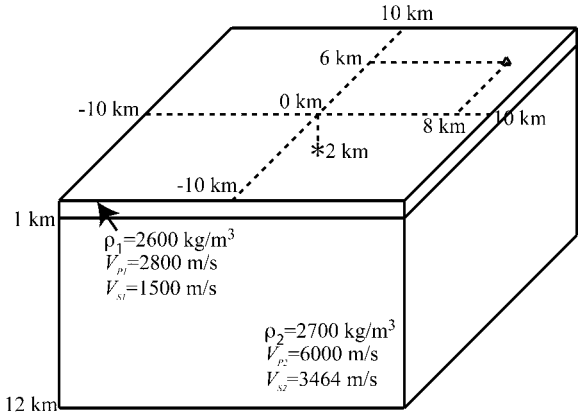

Figure 6. Model of a double-couple point source in a one-layered medium. The source is located at 2 km at depth. The layer is 1 km thick. The small triangle denotes the observation point.

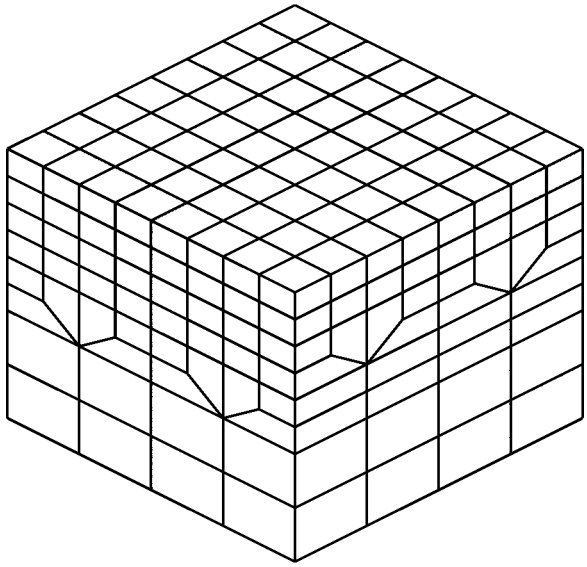

Figure 7. Unstructured hexahedral elements used to define a mesh with smaller elements at the top of the structure, where wave speeds are usually smaller, and with bigger elements at the bottom, where wave speeds are usually larger. We double the element size first in one of the horizontal directions and then in the other. The elements at the bottom are twice as large as the surface elements. The coarsening can be applied as many times as is appropriate. In this way, a roughly constant number of nodes per wavelength is obtained everywhere and the number of degrees of freedom can be dramatically reduced.

Coarse-Grain Modeling of Q

Formulation

Following the underlying principle of the coarse-grain method of modeling Q (Day, 1998; Day and Bradley, 2001), we distribute eight pairs of relaxation times and weights to the center of elements in a spatially periodic manner. Each

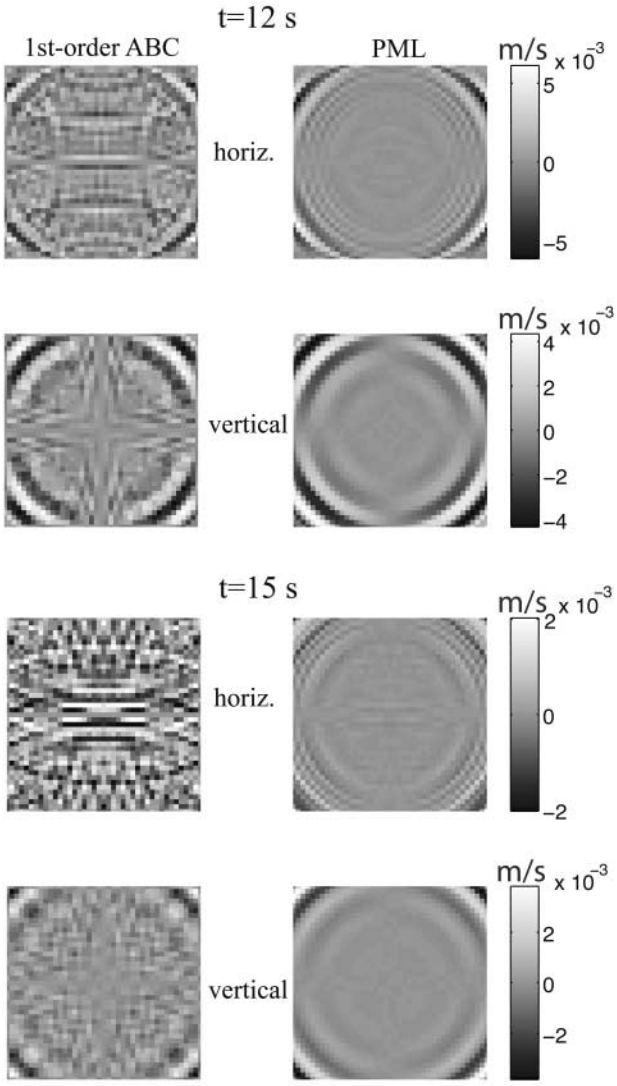

Figure 8. Snapshots of the surface velocities due to a double-couple point source in a one-layered medium with the use of first-order ABC and PML ($\Delta = 6h$). Because of symmetry of the problem, only one horizontal component is shown. The PML absorbs waves well at almost all incidence angles. Large reflections are observed when waves are incident at an oblique angle on the first-order absorbing boundaries. At 15 sec, the reflections from the first-order ABC dominate the solution in the interior region.

element is controlled by only one relaxation mechanism, which is fully determined by the assigned relaxation time and weights. However, the contributions from all neighboring elements together can give a good approximation of a given attenuation model.

It is straightforward to distribute pairs of relaxation time and weight to a structured finite-element mesh. We use

$$k = 1 + (p \bmod 2) + 2(q \bmod 2) + 4(r \bmod 2),$$

which was first used by Day (1998), where p, q, and r are the three spatial indices, and k is the coarse-grain index by which the pair of relaxation time and weights is assigned to the element. Figure 10a shows such a distribution of the coarse-grain index k. It is less straightforward to distribute the index k for the mesh shown in Figure 7. The difficulty lies in the transition zone where unstructured finite elements are used. However, there are still spatial regularities in the mesh. We distribute the index k as periodically as possible in space (shown in Fig. 10b). Each node in the thin unstructured mesh layer is associated with 6, 8, or 12 elements. In the coarse-grain sense, this implementation should give a good approximation of the attenuation model for the periodicity of distribution of index k over a larger coarse-grain unit. Moreover, the total width of the unstructured mesh layer is only one fifth the wavelength so that the effect of the distribution of index k in the unstructured mesh layer in Figure 10b is negligible. This is demonstrated in our numerical example.

There are various ways to get the relaxation time τ_k and weights w_k for each Q. Here we use the approach of Liu and Archuleta (2006). One identical set of relaxation times τ_k is used for any Q between $Q_{\min}$ ($Q_{\min} = 5$) and $Q_{\max} = 5000$). Two sets of weight coefficients w_k and one set of relaxation times τ_k are optimized by applying the simulated annealing algorithm (Liu *et al.*, 1995) to simultaneously fit $Q_{\min}$ and $Q_{\max}$. Using the weight coefficients $w_k^{\min Q}$ for $Q_{\min}$ and $w_k^{\max Q}$ for $Q_{\max}$, the weight coefficient w_k^Q for any constant Q between $Q_{\min}$ and $Q_{\max}$ can be interpolated through an empirical formula (see equation 6 in Liu and Archuleta [2006]).

Once the coarse-grain index k is assigned to each element, the relaxation time τ_k and weights w_k^P and w_k^S can be calculated for a given Q_P (quality factor for P wave) and Q_S (quality factor for S wave), where w_k^P and w_k^S are the weights for Q_P and Q_S, respectively. We define a memory variable σ_{ij}^Q, which is essentially the anelastic stress caused by the assigned relaxation mechanism represented by τ_k, w_k^P, and w_k^S. The memory variable σ_{ij}^Q is governed by

$$\tau_k \sigma_{ij,t}^Q + \sigma_{ij}^Q = 2\mu\varepsilon_{ij} w_k^S + [(\lambda + 2\mu) w_k^P - 2\mu w_k^S]\, \varepsilon_{ll}\delta_{ij}, \tag{19}$$

where ε_{ij} is the elastic strain tensor. Then the total stress σ_{ij} caused by both the elastic stress σ_{ij}^E and the anelastic stress σ_{ij}^Q can be given by

$$\sigma_{ij} = \sigma_{ij}^E - \sigma_{ij}^Q. \tag{20}$$

Equation 19 can be discretized as

$$\sigma_{ij}^{Q,n+1/2} = e^{-\Delta t/\tau_k}\, \sigma_{ij}^{Q,n-1/2} + (1 - e^{-\Delta t/\tau_k}) \{2\mu\varepsilon_{ij} w_k^S + [(\lambda + 2\mu) w_k^P - 2\mu w_k^S]\varepsilon_{ll}\delta_{ij}\}, \tag{21}$$

where n is the temporal index and Δt is the timestep. The expression $\exp(-\Delta t/\tau_k)$ is used in equation (21) rather than

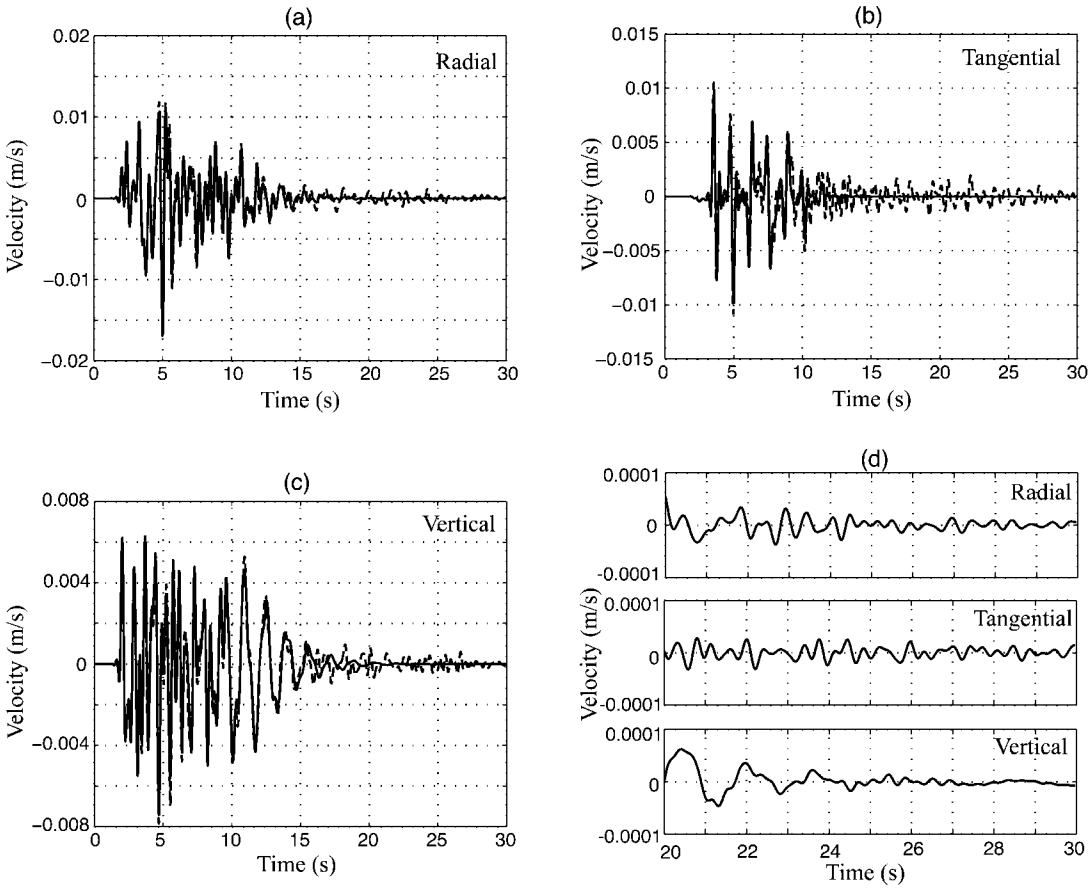

Figure 9. Comparisons of velocity time histories at the observation point for a double-couple point-source in a one-layered medium using PML ($\Delta = 6h$, solid line) and a first-order ABC (dashed line). Large reflections are observed from the first-order absorbing boundary and these reflections affect the solution as early as ~3 sec. No observable reflections are seen from the PML at the normal scale. In (d), we magnify the time histories with the PML after 20 sec by a factor of about 100. The reflection coefficient is about 1%. All results have been low-pass filtered at 3 Hz.

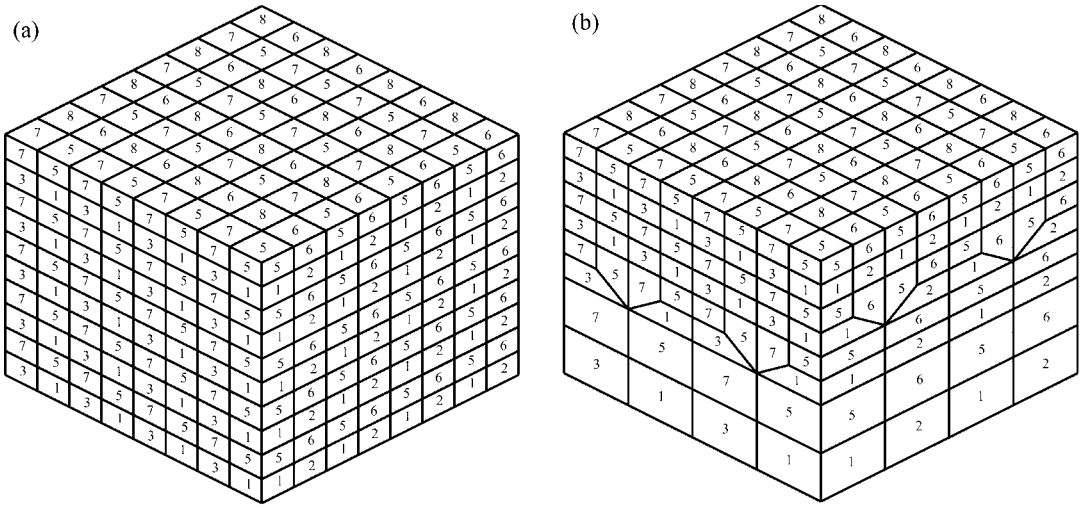

Figure 10. Distribution of the coarse-grain index k in the structured finite-element mesh (a) and the unstructured finite-element mesh (b) (as shown in Fig. 7). Each element is assigned an index k. For clarity, only the indices for surface elements are shown.

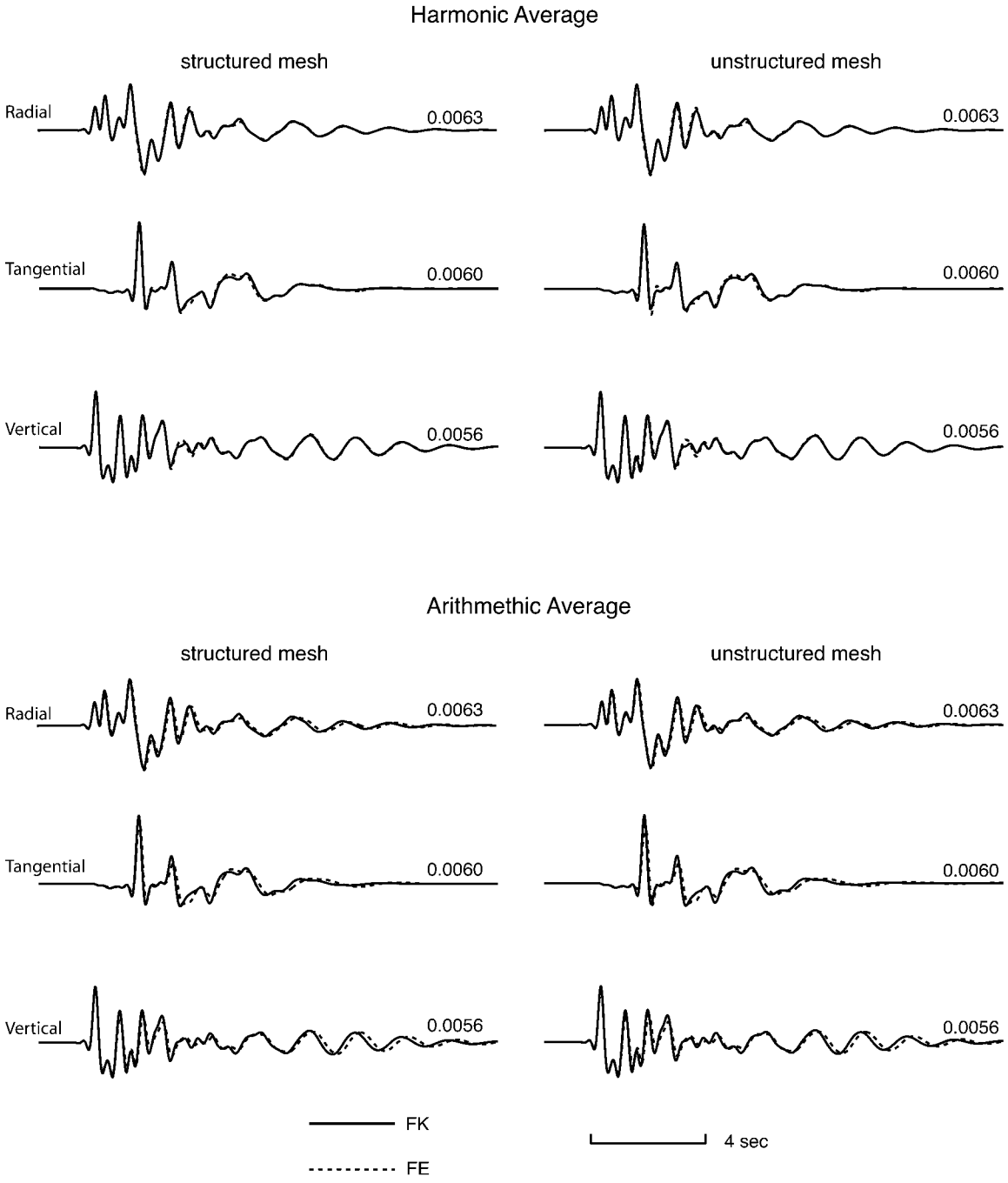

Figure 11. The velocity time histories of the model are compared with analytical solutions at the observation point for a double-couple point source in a one-layered medium with attenuation. We show results for both a structured mesh and an unstructured mesh when the modulus is obtained through a harmonic average and an arithmetic average. Peak velocity (m/sec) for each component is indicated at the upper right of each trace. All results have been lowpass filtered at 3 Hz.

the first diagonal Padé approximant $(1 - 0.5\Delta t/\tau_k)/(1 + 0.5\Delta t/\tau_k)$ because the Padé approximant can be negative when the relaxation time τ_k is very small (Liu and Archuleta, 2006). The stress $\sigma_{ij}^{Q,n}$ can be obtained by the interpolation

$$\sigma_{ij}^{Q,n} = \frac{1}{2}(\sigma_{ij}^{Q,n+1/2} + \sigma_{ij}^{Q,n-1/2}). \quad (22)$$

Once the stress $\sigma_{ij}^{Q,n}$ is obtained, we add it to the elastic stress using equation (20), which can then be distributed through the B matrix to the elemental nodal forces as in previous implementations.

Numerical Example

We test our finite-element implementation of the coarse-grain modeling of Q in the same model used earlier, as shown in Figure 6. Except for attenuations in the velocity structure, this model has the same parameters as the model we used in the Modeling of PML section. For the top layer, we use $Q_P = 20$ and $Q_S = 10$. For the half-space, we use $Q_P = 100$ and $Q_S = 50$. We implement the coarse-grain approach in both a structured finite-element mesh and an unstructured finite-element mesh with the distributions of the coarse-grain index as shown in Figure 10. We set the reference frequency at 1.0 Hz. The analytical solution is calculated by the frequency-wavenumber (FK) method.

In the coarse-grain approach, the relaxation times and relaxation weights are determined so that the average modulus over the coarse-grained volume across eight adjacent elements gives a Q model that matches the target Q. The average modulus is conventionally calculated through an arithmetic average. However, Graves and Day (2003) showed that the harmonic average of the modulus works better for the coarse-grain system. We test both the arithmetic average and harmonic average in the example.

Figure 11 shows the three velocity components at the observation point, 10 km from the epicenter. The waveforms obtained through the harmonic average of modulus show an excellent agreement with the analytical solutions in both the structured and unstructured mesh. In the modulus calculated with an arithmetic average, the amplitudes of the waveforms are well reproduced, but the phases show mismatches. This confirms the results of Graves and Day (2003), that is, the harmonic average of modulus is more accurate in the coarse-grain approach, especially when Q is small. The unstructured mesh generates almost identical results with the structured mesh in both averaging schemes, which demonstrates the high accuracy of our implementation of the coarse-grain approach in the unstructured mesh.

Conclusion

We have presented a finite-element implementation of PML and the coarse-grain method for modeling Q. The one-point integration in the finite-element method gives rise to a natural implementation of the velocity-stress formulation of PML. It allows the use of both regular and irregular elements. By testing Lamb's problem and wave propagation in a layered velocity structure, the PML shows excellent performance: both surface waves and body waves are well absorbed with no observable reflections. The one-point integration also leads to an easy incorporation of the coarse-grain approach for modeling Q. Anelastic wave propagations using the coarse-grain approach with both a structured and unstructured mesh show excellent agreement with analytical solutions when the viscoelastic modulus is calculated through a harmonic average over the coarse-grain unit. Our approach greatly expands the applicability of PML and the coarse-grain approach for modeling Q and can be easily implemented in other numerical methods.

Acknowledgments

We are very grateful to Morgan Page for revising several drafts of this article and Ralph Archuleta for helpful discussions. Two anonymous reviewers gave constructive reviews. This work is supported by the Southern California Earthquake Center (SCEC), by NSF ITR through Award EAR-0122464 (The SCEC Community Modeling Environment [SCEC/CME]: An Information Infrastructure for System-Level Earthquake Research), and by IGPP LANL Grant 04-08-16L-1532. SCEC is funded by NSF Cooperative Agreement EAR-0106924 and USGS Cooperative Agreement 02HQAG0008. This is SCEC contribution no. 973 and Institute for Crustal Studies contribution no. 0732.

References

Aagaard, B., T. H. Heaton, and J. F. Hall (2001). Dynamic earthquake ruptures in the presence of lithostatic normal stresses: Implications for friction models and heat production, *Bull. Seism. Soc. Am.* **91,** 1765–1796.

Aki, K., and P. G. Richards (2002). *Quantitative Seismology*, University Science Books, Sausalito, California.

Anderson, G., B. Aagaard, and K. Hudnut (2003). Fault interactions and large complex earthquakes in the Los Angeles area, *Science* **302,** 1946–1949.

Archuleta, R. J., and G. A. Frazier (1978). Three-dimensional numerical simulations of dynamic faulting in a half-space, *Bull. Seism. Soc. Am.* **68,** 541–572.

Bao, H., J. Bielak, O. Ghattas, L. F. Kallivokas, D. R. O'Hallaron, J. R. Shewchuk, and J. Xu (1998). Large-scale simulation of elastic wave propagation in heterogeneous media on parallel computers, *Comput. Methods Appl. Mech. Eng.* **152,** 85–102.

Basu, U., and A. K. Chopra (2004). Perfectly matched layers for transient elastodynamics of unbounded domains, *Int. J. Numer. Methods Eng.* **59,** 1039–1074.

Belytschko, T., J. S. Ong, W. K. Liu, and J. M. Kennedy (1984). Hourglass control in linear and nonlinear problems, *Comput. Methods Appl. Mech. Eng.* **43,** 251–276.

Bérenger, J. P. (1994). A perfectly matched layter for the absorption of electromagnetic waves, *J. Comp. Phys.* **114,** 185–200.

Bérenger, J. P. (1996). Three-dimensional perfectly matched layer for the absorption of electromagnetic waves, *J. Comp. Phys.* **127,** 363–379.

Carcione, J. M., D. Kosloff, and R. Kosloff (1988). Wave propagation in a linear viscoacoustic medium, *Geophys. J. R. Astr. Soc.* **93,** 393–407.

Clayton, R., and B. Engquist (1977). Absorbing boundary conditions for acoustic and elastic wave equations, *Bull. Seism. Soc. Am.* **67,** 1529–1540.

Collino, R., and C. Tsogka (2001). Application of the PML absorbing layer model to the linear elastodynamic problem in anisotropic heterogeneous media, *Geophysics* **66,** 294–307.

Day, S. M. (1982). Three-dimensional simulation of spontaneous rupture: The effect of nonuniform prestress, *Bull. Seism. Soc. Am.* **72,** 1881–1902.

Day, S. M. (1998). Efficient simulation of constant Q using coarse-grained memory variables, *Bull. Seism. Soc. Am.* **88,** 1051–1062.

Day, S. M., and C. R. Bradley (2001). Memory efficient simulation of anelastic wave propagation, *Bull. Seism. Soc. Am.* **91,** 520–531.

Day, S. M., and J. B. Minster (1984). Numerical simulation of attenuated wavefields using a Padé approximant method, *Geophys. J. R. Astr. Soc.* **78,** 105–118.

Day, S. M., L. A. Dalguer, N. Lapusta, and Y. Liu (2005). Comparison of finite difference and boundary integral solutions to three-dimensional spontaneous rupture, *J. Geophys. Res.* **110,** B12307, doi 10.1029/2005JB003813.

Emmerich, H., and M. Korn (1987). Incorporation of attenuation into time domain computations of seismic wave fields, *Geophysics* **52,** 1252–1264.

Festa, G., and S. Nielsen (2003). PML absorbing boundaries, *Bull. Seism. Soc. Am.* **93,** 891–903.

Festa, G., and J.-P. Vilotte (2005). The Newmark scheme as velocity-stress time-staggering: an efficient PML implementation for spectral element simulations of elastodynamics, *Geophys. J. Int.* **161,** 789–812.

Flanagan, D. P., and T. Belytschko (1981). A uniform strain hexahedron and quadrilateral with orthogonal hourglass control, *Int. J. Numer. Methods Eng.* **17,** 679–706.

Gourdreau, G. L., and J. O. Hallquist (1982). Recent developements in large scale finite elements Lagrangian hydrocode technology, *Comput. Methods Appl. Mech. Eng.* **33,** 725–757.

Graves, R. W., and S. M. Day (2003). Stability and accuracy analysis of coarse-grain viscoelastic simulations, *Bull. Seism. Soc. Am.* **93,** 283–300.

Hastings, F., J. B. Schneider, and S. L. Broschat (1996). Application of the perfectly matched layer (PML) absorbing boundary condition to elastic wave propagation, *J. Acoust. Soc. Am.* **100,** 3061–3069.

Higdon, R. L. (1991). Absorbing boundary conditions for elastic waves, *Geophysics* **56,** 639–666.

Hisada, Y., H. Bao, J. Bielak, O. Ghattas, and D. O'Hallaron (1998). Simulations of long-period ground motions during the 1995 Hyoto-Ken Nanbu (Kobe) earthquake using a 3D finite element method, in *2nd International Symposium on Effect of Surface Geology on Seismic Motion*, Yokohama, Japan, 59–66.

Hughes, T. J. R. (1987). *Finite Element Method—Linear Static and Dynamic Finite Element Analysis*, Prentice-Hall, Englewood Cliffs, New Jersey.

Kim, E., J. Bielak, and O. Ghattas (2003). Large-scale Northridge earthquake simulation using octree-based multireslution mesh method, in *Proceedings of the 16th ASCE Engineering Mechanics Conference*, Seattle, Washington, July 2003.

Koketsu, K., H. Fujiwara, and Y. Ikegami (2004). Finite-element simulation of seismic ground motion with a voxel mesh, *Pure Appl. Geophys.* **161,** 2183–2198.

Komatitsch, D., and J. Tromp (1999). Introduction to the spectral-element method for 3-D seismic wave propagation, *Geophys. J. Int.* **139,** 806–822.

Komatitsch, D., and J. Tromp (2002a). Spectral-element simulations of global seismic wave propagation. I. Validation, *Geophys. J. Int.* **149,** 390–412.

Komatitsch, D., and J. Tromp (2002b). Spectral-element simulations of global seismic wave propagation. II. Three-dimensional models, oceans, rotation and self-gravitation, *Geophys. J. Int.* **150,** 303–318.

Komatitsch, D., and J. Tromp (2003). A perfectly matched layer absorbing boundary condition for the second-order seismic wave equation, *Geophys. J. Int.* **154,** 146–153.

Komatitsch, D., Q. Liu, J. Tromp, P. Süss, C. Stidham, and J. Shaw (2004). Simulations of ground motion in the Los Angeles basin based upon the spectral-element method, *Bull. Seism. Soc. Am.* **94,** 187–206.

Komatitsch, D., J. Ritsema, and J. Tromp (2002). The spectral-element method, Beowulf computing and global seismology, *Science* **298,** 1737–1742.

Kosloff, D., and G. A. Frazier (1978). Treatment of hourglass patterns in low order finite element codes, *Int. J. Numer. Anal. Methods Geomech.* **2,** 57–72.

Liu, P., and R. J. Archuleta (2006). Efficiently modeling of *Q* for 3D numerical simulation of wave propagation, *Bull. Seism. Soc. Am.* **96,** no. 4, 1352–1358.

Liu, R., D. L. Anderson, and H. Kanamori (1976). Velocity dispersion due to anelasticity: implication for seismology and mantle composition, *Geophys. J. R. Astr. Soc.* **47,** 41–58.

Liu, P., S. Hartzell, and W. Stephenson (1995). Nonlinear multiparameter inversion using a hybrid global search algorithm: applications in reflection seismology, *Geophys. J. Int.* **122,** 991–1000.

Lysmer, J., and L. A. Drake (1972). A finite element method for seismology, in *Methods in Computational Physics*, Vol. 11, B. Alder, S. Fernbach, and B. A. Bolt (Editors), Academic Press, New York.

Lysmer, J., and R. L. Kuhlmeryer (1969). Finite dynamic model for infinite media. *J. Eng. Mech.* **95,** 859–877.

Marcinkovich, C., and K. Olsen (2003). On the implementation of perfectly matched layers in a three-dimensional fourth-order velocity-stress finite difference scheme, *J. Geophys. Res.* **108,** no. B(5), 2276, doi 10.1029/2002JB002235.

Oglesby, D. D., R. J. Archuleta, and S. B. Nielsen (1998). Earthquakes on dipping faults: the effects of broken symmetry, *Science* **280,** 1055–1059.

Pereyra, V., E. Richardson, and S. E. Zarantonello (1992). Large scale calculations of 3D elastic wave propagation in a complex geology, in *Proceedings Supercomputing '92*, 301–309.

Robertson, J. O. A., J. O. Blanch, and W. W. Symes (1994). Viscoelastic finite-difference modeling, *Geophysics* **59,** 1444–1456.

Smith, W. D. (1975). The application of finite element analysis to body wave propgation problems, *Geophys. J.* **42,** 747–768.

Wilson, E. L., R. J. Taylor, W. P. Doherty, and J. Ghaboussi (1973). Incompatible displacement models, in *Numerical and Computer Methods in Structural Mechanics*, S. J. Fenves, N. Perrone, A. R. Robinson, and W. C. Schnobrich (Editors), Academic Press, New York, 43–57.

Xu, T., and G. A. McMechan (1998). Efficient 3D viscoelastic modeling with application to near-surface land seismic data, *Geophysics* **63,** 601–612.

Appendix A

Determination of the *B* Matrix

Following the isoparametric transformation, the derivatives with respect to x, y, and z are related to the derivatives with respect to ξ, η, and ζ through

$$\begin{Bmatrix} \partial_\xi \\ \partial_\eta \\ \partial_\zeta \end{Bmatrix} = J \begin{Bmatrix} \partial_x \\ \partial_y \\ \partial_z \end{Bmatrix} = \begin{bmatrix} \frac{\partial x}{\partial \xi} & \frac{\partial y}{\partial \xi} & \frac{\partial z}{\partial \xi} \\ \frac{\partial x}{\partial \eta} & \frac{\partial y}{\partial \eta} & \frac{\partial z}{\partial \eta} \\ \frac{\partial x}{\partial \xi} & \frac{\partial y}{\partial \xi} & \frac{\partial z}{\partial \xi} \end{bmatrix} \begin{Bmatrix} \partial_x \\ \partial_y \\ \partial_z \end{Bmatrix},$$

where the Jocobian matrix J is a function of ξ, η, and ζ.

It can be shown that

$$J(0,\,0,\,0) \;=\; \frac{1}{8}\begin{bmatrix} x_1-x_2-x_3+x_4+x_5-x_6-x_7+x_8 & y_1-y_2-y_3+y_4+y_5-y_6-y_7+y_8 & z_1-z_2-z_3+z_4+z_5-z_6-z_7+z_8 \\ x_1+x_2-x_3-x_4+x_5+x_6-x_7-x_8 & y_1+y_2-y_3-y_4+y_5+y_6-y_7-y_8 & z_1+z_2-z_3-z_4+z_5+z_6-z_7-z_8 \\ x_1+x_2+x_3+x_4-x_5-x_6-x_7-x_8 & y_1+y_2+y_3+y_4-y_5-y_6-y_7-y_8 & z_1+z_2+z_3+z_4-z_5-z_6-z_7-z_8 \end{bmatrix}$$

and the element volume $V = 8|J(0,0,0)|$.

By calculating J^{-1} (0,0,0), we can determine the B matrix following equation (1):

$$B_{11} = \frac{1}{16V}\left[y_{82}(z_{54}+z_{63}) + y_{35}(z_{42}+z_{86}) + y_{46}(z_{52}+z_{83})\right],$$

$$B_{12} = \frac{1}{16V}\left[y_{53}(z_{61}+z_{74}) + y_{46}(z_{13}+z_{57}) + y_{17}(z_{63}+z_{54})\right],$$

$$B_{13} = \frac{1}{16V}\left[y_{64}(z_{72}+z_{81}) + y_{17}(z_{24}+z_{68}) + y_{28}(z_{74}+z_{61})\right],$$

$$B_{14} = \frac{1}{16V}\left[y_{71}(z_{83}+z_{52}) + y_{28}(z_{31}+z_{75}) + y_{35}(z_{81}+z_{72})\right],$$

$$B_{21} = \frac{1}{16V}\left[z_{82}(x_{54}+x_{63}) + z_{35}(x_{42}+x_{86}) + z_{46}(x_{52}+x_{83})\right],$$

$$B_{22} = \frac{1}{16V}\left[z_{53}(x_{61}+x_{74}) + z_{46}(x_{13}+x_{57}) + z_{17}(x_{63}+x_{54})\right],$$

$$B_{23} = \frac{1}{16V}\left[z_{64}(x_{72}+x_{81}) + z_{17}(x_{24}+x_{68}) + z_{28}(x_{74}+x_{61})\right],$$

$$B_{24} = \frac{1}{16V}\left[z_{71}(x_{83}+x_{52}) + z_{28}(x_{31}+x_{75}) + z_{35}(x_{81}+x_{72})\right],$$

$$B_{31} = \frac{1}{16V}\left[x_{82}(y_{54}+y_{63}) + x_{35}(y_{42}+y_{86}) + x_{46}(y_{52}+y_{83})\right],$$

$$B_{32} = \frac{1}{16V}\left[x_{53}(y_{61}+y_{74}) + x_{46}(y_{13}+y_{57}) + x_{17}(y_{63}+y_{54})\right],$$

$$B_{33} = \frac{1}{16V}\left[x_{64}(y_{72}+y_{81}) + x_{17}(y_{24}+y_{68}) + x_{28}(y_{74}+y_{61})\right],$$

$$B_{34} = \frac{1}{16V}\left[x_{71}(y_{83}+y_{52}) + x_{28}(y_{31}+y_{75}) + x_{35}(y_{81}+y_{72})\right],$$

$$B_{15} = -B_{13},\quad B_{25} = -B_{23},\quad B_{35} = -B_{33},$$
$$B_{16} = -B_{14},\quad B_{26} = -B_{24},\quad B_{36} = -B_{34},$$
$$B_{17} = -B_{11},\quad B_{27} = -B_{21},\quad B_{37} = -B_{31},$$
$$B_{18} = -B_{12},\quad B_{28} = -B_{22},\quad B_{38} = -B_{32},$$

where $x_{IJ} = x_I - x_J$, $y_{IJ} = y_I - y_J$, and $z_{IJ} = z_I - z_J$.

Appendix B

Computational Sequence of the One-Point Integration Algorithm with Both the Viscous and Stiffness Hourglass Control

1. The global internal elastic force vector $F_i^{\text{elastic},n-1}$ and global velocity vector $V_i^{n-1/2}$ are known at time $t = n\Delta t$, where n is the temporal index and Δt is the timestep.
2. Loop over all the elements.
   a. Calculate the element volume V.
   b. Calculate the B matrix from Appendix A.
   c. Calculate the velocity gradient $v_{i,j}$ from equation (2).
   d. Calculate the stress rate σ_{ij} from equation (4).
   e. Calculate the nodal force rate $\dot{f}_{jl}^{\text{stress}}$ caused by the stress rate using equation (5).
   f. Calculate the stiffness hourglass force rate $\dot{f}_{jl}^{ehg}$ using equation (8).
   g. Calculate the element elastic-force rate $\dot{f}_{jl}^{\text{elastic}}$ from equation (9).
   h. Update the element elastic-force $f_{jl}^{\text{elastic},n} = f_{jl}^{\text{elastic},n-1} + \dot{f}_{jl}^{\text{elastic}}\Delta t$ and add it to the global internal elastic-force vector $F_i^{\text{elastic},n}$.
   i. Calculate the viscous hourglass force f_{jl}^{vhg} from equation (7) and add it to the global viscous hourglass-force vector $F_i^{vhg,n}$.
3. Update the velocity vector $V_i^{n+1/2} = V_i^{n-1/2} + (F_i^{\text{ext},n} - F_i^{\text{elastic},n} - F_i^{vhg,n})/M\Delta t$, where $F_i^{\text{ext},n}$ is the global external-force vector at $t = n\Delta t$ and M is the global lumped mass vector.
4. Go to step 1 to begin the next timestep.

Department of Earth Science and Institute for Crustal Studies
University of California, Santa Barbara
Santa Barbara, California 93106
(S.M.)

Institute for Crustal Studies
University of California, Santa Barbara
Santa Barbara, California 93106
(P.L.)

Manuscript received 2 November 2005.